SEVENTH FRAMEWORK PROGRAMME
THEME FP7-ICT-2007-2
Information and Communication Technologies

Project # 224197 – TUMESA

MEMS Tuneable Metamaterials for Smart Wireless Applications

Deliverable 1.6

Fabricated and characterised smart reflective beam steering surface on a chip

Contractual Date of Delivery to the CEC: August 31st, 2011

Actual Date of Delivery to the CEC: November 7th, 2011

Author: Zhou Du, Juha Ala-Laurinaho, Dmitri Chicherin, Mikael Sterner, Joachim Oberhammer

Participants: AALTO, KTH

Work package: WP1, MEMS Tuneable Metamaterials for Low-Loss Single Chip Beam Steering

Est. person months: 20 person-months

Security: PU

Nature: R, P

Version: 1.0

Total number of pages: 20

Abstract:

MEMS based tuneable high-impedance surface (HIS) can be used for beam steering elements in different forms: as a reflection type phase shifter, as a phase shifter based on a dielectric waveguide, or as a reflective single chip beam steering surface. In this report, design of the high-impedance surfaces for beam steering is reviewed and simulation results are shown. Some samples of HIS chips produced during the project are tested. Also, a reflection type phase shifter based on MEMS-based high-impedance surface is tested.

Keyword list: MEMS tuneable high-impedance surface, phase shifter

Executive Summary

Present deliverable consists of four chapters and a conclusion.

First, a review of the design of the proposed MEMS-based tuneable high-impedance surface is given, as well as brief description of tuneability of the unit cell structure, and simulated antenna beams. Second, the manufacturing processes for the high-impedance surfaces during the TUMESA project are summarised. Third, the quasi-optical measurements of the beam-steering HIS chips are presented. Fourth, the measurement results of the reflection type phase shifter based on MEMS-based high-impedance surface are presented.

Conclusion summarises the deliverable.

Full description of deliverable content

Contents:

1. Review: MEMS-based tuneable high-impedance surface

As it was described in Deliverable 1.1, we have identified MEMS-based high-impedance surfaces (HIS) as a suitable type of metamaterials for the application being developed in the frame of TUMESA project. The proposed MEMS tuneable HIS is a multi-layer structure, in contrast to original mushroom structure, and it consists of an array of electrically small MEMS parallel-plate capacitors, in which the top plate is suspended by springs. The basic idea of the proposed variable capacitor is that application of a bias voltage between the membrane and the bottom plate of the MEMS varactor changes the distance between them, which in turn changes the effective capacitance of the whole structure affecting the resonance frequency of the HIS.
The schematic design of the single unit cell of the MEMS-based HIS is shown in Fig. 1, where dimensions are: w = 130μm, Mx = 70μm, My = 110μm, b = 350μm and h = 110μm. The upper membrane, which is formed by three layers (Au + Si + Au), is placed at a certain distance *g* from the lower metal patches. The bias voltage is applied between the membrane and the lower patches.

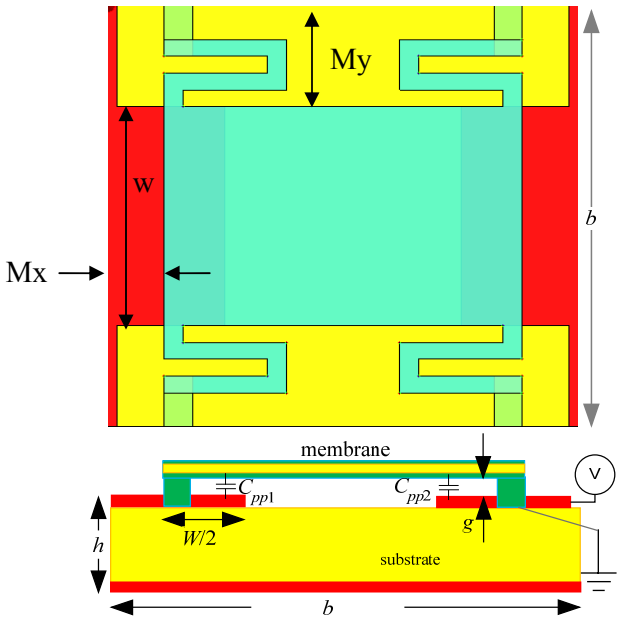

Fig. 1 Top and side view of the schematic design of MEMS tuneable high-impedance surface, not to scale.

The unit cell is much smaller than the wavelength of the incident field, thus the HIS can be analysed in terms of equivalent input impedance. The input impedance of MEMS-based HIS can be interpreted as the parallel connection of the capacitive grid impedance Z_g due to the adjacent metal patches, the capacitive impedance Z_{pp} due to the parallel-plate capacitor between the upper membrane and the lower patches, and the inductive input impedance Z_s due to the thin grounded dielectric layer. The equivalent transmission line model is shown in Fig. 2

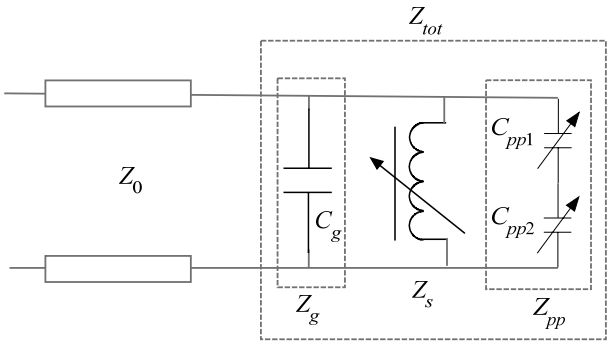

Fig. 2 Equivalent circuit of the single unit cell structure.

The HIS is a resonance structure, and at the resonance frequency the phase of the reflection coefficient becomes 0°. From the theoretical point of view, the reflection phase of a tuneable HIS at any fixed frequency varies continuously from -180° to +180° with continuous change of the capacitance value. Since the HIS is a periodic structure, its electromagnetic performance can be simulated with a simplified model of a single unit cell with appropriate boundary conditions. We simulated the structure with 110µm substrate thickness using full wave 3-D simulation software Ansoft HFSS, to analyze the tuneability range. Fig. 3 shows simulation results of the reflection phase of the HIS unit cell for different values of the gap of the MEMS varactor. It indicates that, by varying the gap to certain values, the resonant frequency is tuned from approximately 70 GHz to 100 GHz.

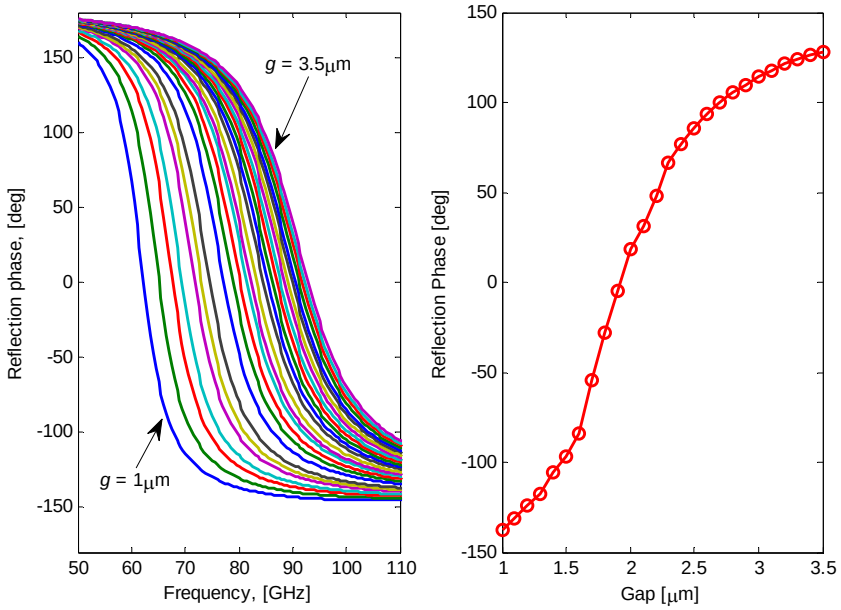

Fig. 3 Reflection phase for single unit cell with 110 µm substrate thickness as a function of frequency (lhs) and gap at 80 GHz (rhs, structure with electrode), simulated.

MEMS tuneable HIS can be used for electronic reflective beam steering by inducing reconfigurable surface impedance by applying different bias voltage to different rows of elements of the MEMS varactor array. Since full-wave simulation of electrically large reflective surface with electrically small features of MEMS varactors is computationally practically impossible, a simplified model of a surface with strips formed by 40 impedance elements of 0.35 x 0.35 mm^2 is used. If all strips have the same impedance, the angle of the reflected beam is equal to the angle of the incident beam. Configuring the surface so that different strips have different impedances and different phase of the reflection coefficient, the reflected beam can be steered by changing the gradient of the surface impedance. To reflect a beam of normal incidence in the direction θ from normal, the phase difference between adjacent strips should be: $\Delta\Phi = kbsin(\theta)$.

The strip line structures are placed in the open boundary conditions, and the radiation pattern of the reflected beam is simulated for two different incident angles: normal incidence and 45° incidence. Fig. 4 shows an example of the required reflection phase and impedances of the strips with incident angle from 45°. In order to model a planar array condition, 20 arrays with 0 phase shift are added in the z-direction. Far-field at 80 GHz is monitored to obtain the normalized radiation pattern. When a wave impinges to a flat surface obliquely, it will generate backward and forward reflected wave (see Fig. 5). These waves contribute to the side lobe level at particular angles. In the model, we assume the initial phase of the first strip to be 90°. This initial phase influences the impedance value of each element. However, it only affects a little to the side lobe level, because of the field averaging, which has been verified by numerical simulations.

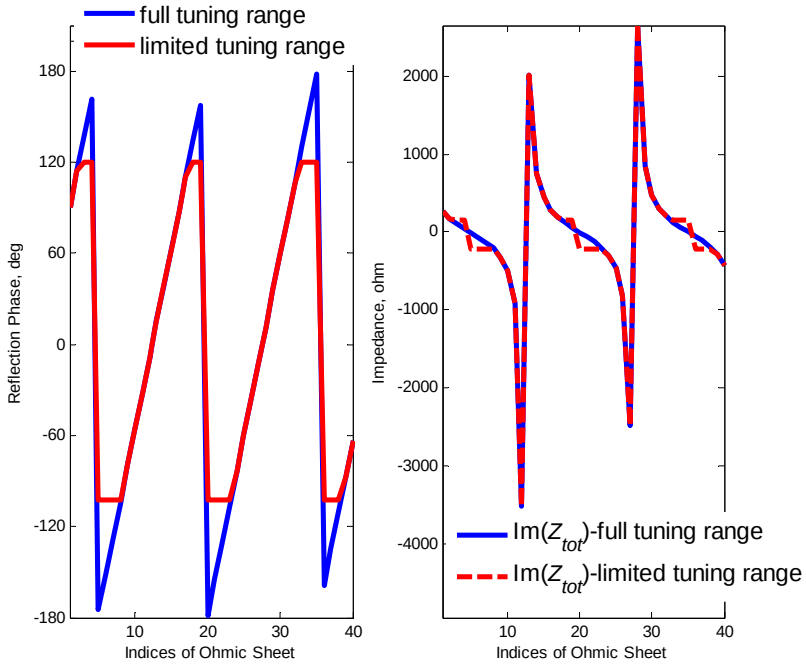

Fig. 4 The required reflection phase impedances with incident angle of 45° and the reflective beam to be steered to 0°.

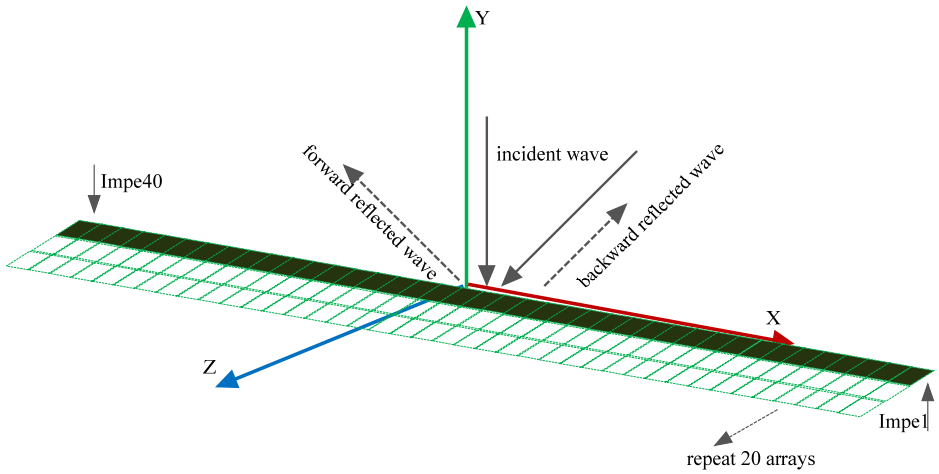

Fig. 5 40 impedance elements in the open boundary conditions, normal and 45° off broadside incidence are excited to the surface.

A series of normalized radiation patterns for several steering angles are shown in Fig. 6. As a reference, we have also simulated the radiation pattern of the surface with equal impedance (50 ohm resistance). For oblique incidence of 45° the strongest lobe is the main steering lobe according to the programmed reflection angle, i.e. -30° and 0°, see Fig. 6(a). A strong forward reflected wave side lobe can be observed through these simulation results, which is due to the specular reflection law occurred when a wave impinges to a flat surface. The limited tuning range does not produce a perfectly linear phase gradient, as the phase is truncated at extreme values. This problem is most severe at the 2π discontinuities, and as a result the radiation patterns have additional higher backward reflected wave side lobes (Fig. 6(a)). Opposite phase gradient is needed when beam is steered to the opposite direction. The surface can steer to any angle between these extremes, i.e. ±45°. To illustrate the effect of the number of the impedance elements on radiation pattern, performances of 60 and 80 elements are added as shown in Fig. 7. Significant decrease of the backward reflected wave side lobe level has been achieved when increasing the number of impedance elements from 40 to 80, while the forward wave side lobe level remains the same.

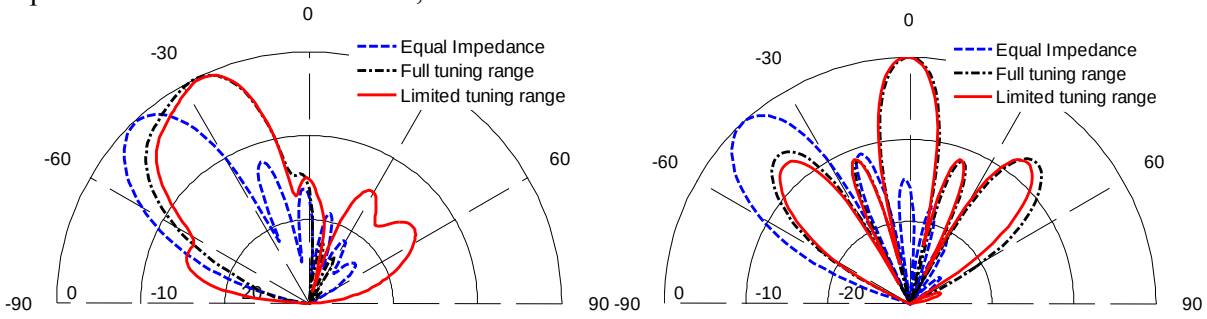

Fig. 6 The normalized radiation pattern at 80 GHz with incident angle from 45° for the surface which is programmed for: (a) -30°, (b) 0°.

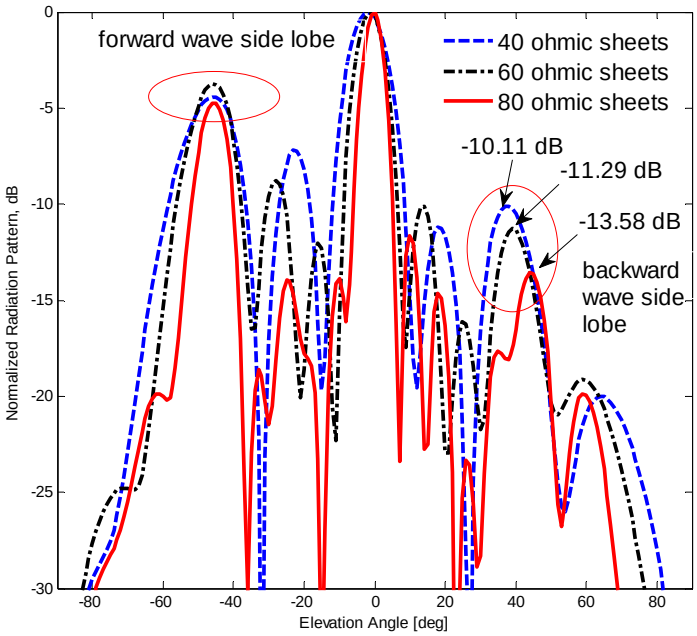

Fig. 7 The normalized radiation pattern at 80 GHz for the surface which is programmed for 0° with incident angle from 45° (using limited tuning range).

2. Fabrication of high impedance surfaces

The basic fabrication process of the high impedance surfaces has been explained in deliverables D4.1 and D4.2. Also the fabrication process for the large arrays for beam steering was discussed in deliverable D4.4, including the problems pertaining to the yield of making big arrays. The following fabrication runs of large arrays were planned and carried out during the project:

- Sharp run 1. Completed 2009-03. The first run with high resistivity silicon as dielectric layer. Achieved a good surface of the substrate, due to good CTE matching of the silicon substrates compared to previous glass materials.
- Sharp run 2. Completed 2009-07. A resist based planarization scheme was developed to improved adhesion of the thin transferred membrane layer, achieving a much higher bonding yield over the wafer.
- Sharp run 3. Completed 2009-08. Test structures were included for characterizing the reliability and curvature of the thin membranes.
- Sharp run 4. Completed 2010-01. New run with optimized process to improved yield.
- Sharp run 5. Completed 2010-10. Further process optimization for the large arrays.

During the last months of the project, KTH has attempted a final fabrication run, with unchanged design but some minor modifications in the process flow, for improved yield and for delivering the final chips for test purpose to AALTO. This fabrication run had to be carried out under tough time restrictions in an attempt to deliver large area high impedance surfaces in time for measuring before the project end. Two key processes were not available in these time constraints. KTH went to other fabrication facilities but processes there were not sufficiently developed to meet the fabrication specifications, despite efforts to rework the lost material.

Additional rework activities were performed with large arrays from previous fabrication runs which were then additionally sent to AALTO for further quasi-optical measurements. However, these backup large arrays from previous fabrication runs were not deemed fit for tuning on array level, and thus could not be used to test the beam steering system.

3. Measurement of the MEMS-based HIS

3.1 Quasioptical measurements of the MEMS-based HIS

Although the fabrication of the large-scale tuneable high impedance surfaces was not successful, some fabricated samples were measured in order to study the effect of the incidence angle on the operation of the surfaces. The HIS samples are 200 × 52 arrays of unit cells with 350μm periodic length, i.e. the size of the chips is 70 mm × 18 mm. Totally four samples of beam steering chips are received from KTH, which are abbreviated as HIS1, HIS2, HIS3, and HIS4 (see Fig. 8). An aluminum plate with the same dimension of HIS is also measured as the reference. The description of the samples is as follows:

1. HIS1: free etched, degraded plating (some strips of membranes peel off)
2. HIS2: partially free etched, static
3. HIS3: free etched, but with burnt resist keeping it static
4. HIS4: same as 3, but not free etched

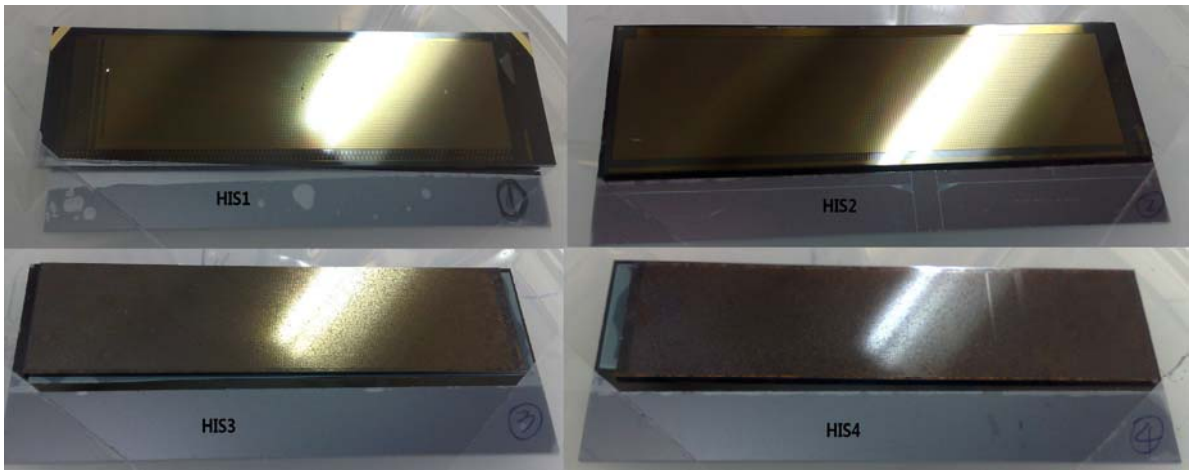

Fig. 8 Four samples of beam steering chips.

A quasi-optical measurement setup is built for the measurement of high impedance surface (HIS) with three different incident angles, which are 30°, 45° and 60° with respect to the normal direction of the HIS (see Fig. 9 and Fig. 10). Two standard horn antennas are mounted at test port 1 and 2 and thus acting as the transmitting and receiving antennas. In addition, two parabolic reflectors are used to collimate and focus the transmitting waves. With this setup the HIS is illuminated with a planar wave-front. The HIS or aluminum plate is fixed on the rotator, and the incident angle is defined by tuning the rotator. Meanwhile, a flat mirror is mounted on a carrier rail in order to position it properly with respect to the corresponding incident angle. With the proposed setup, for a chosen incident angle and a fixed polarization (TE mode), the transmission coefficient of the HIS (or aluminum plate) under test is recorded through two test ports by the HP8510 vector network analyzer.

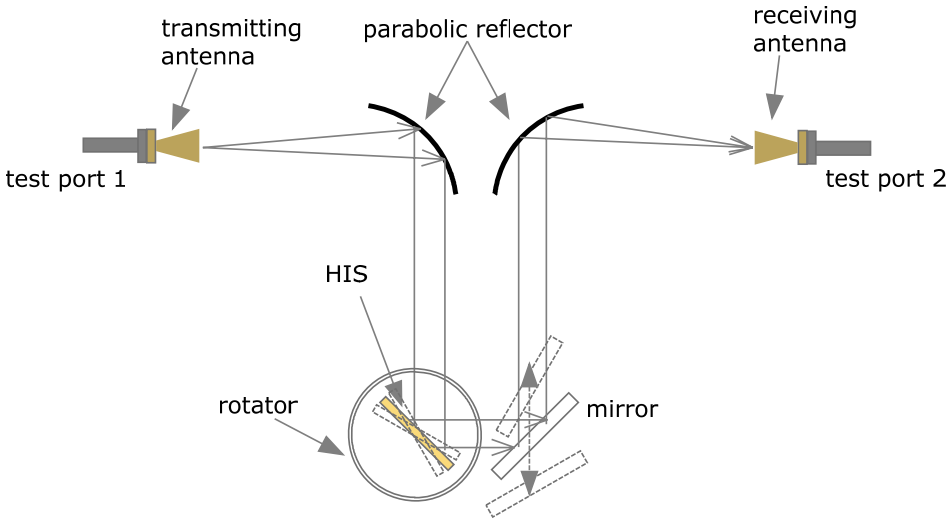

Fig. 9 Schematic design of the quasi-optical measurement setup.

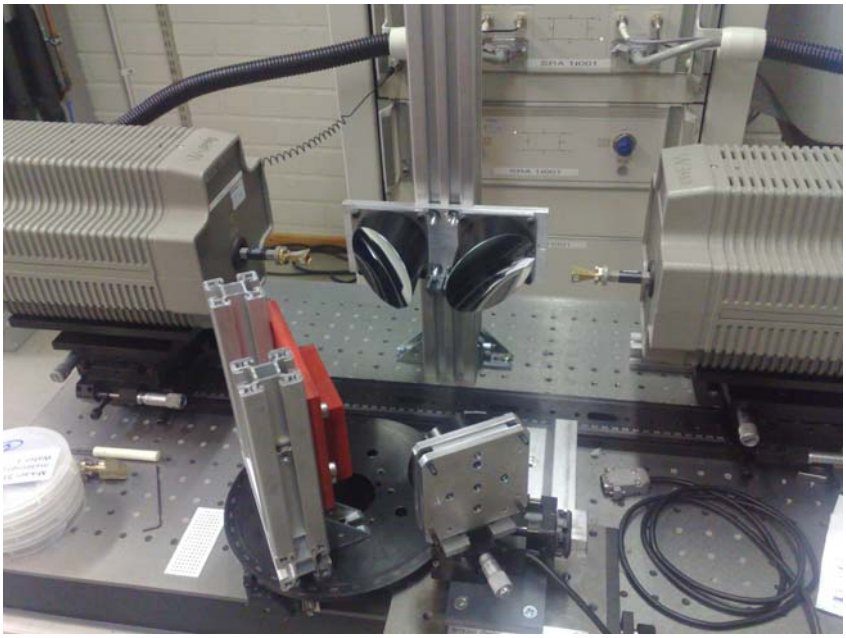

Fig. 10 Photograph of the quasi-optical measurement setup.

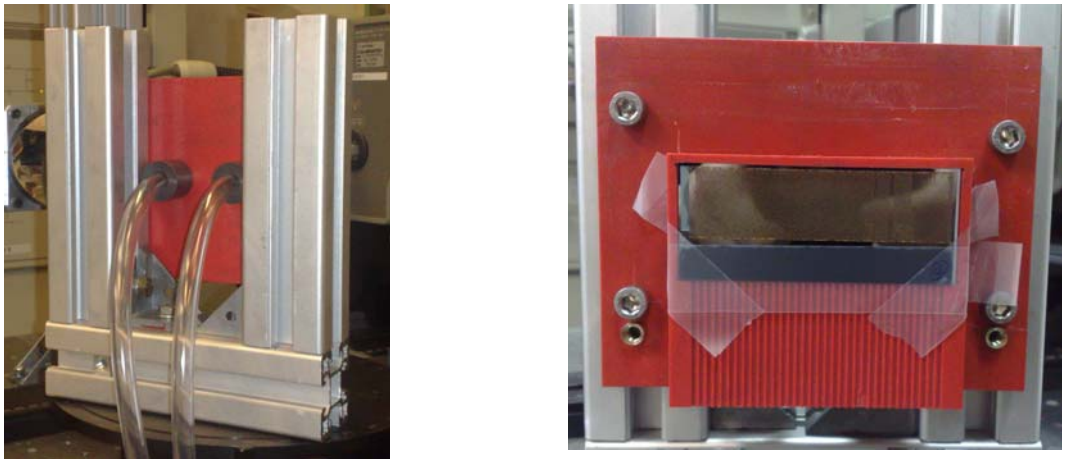

Fig. 11 Photograph of the HIS chip holder made of PVC plastic. Vacuum section (hoses are shown in lhs) is used to attach the chip on the holder, while tapes are used for handling the chip.

Figs. 12-16 show the measurement results of the S21 for the aluminium plate and for each of the HIS chips with different incident angles. The measured HIS chip results are calibrated with the measurement results of the aluminium plate. The measurements results do not indicate resonances within the frequency range of the measurements. However, these measurements show that the specular reflection for the HIS surfaces is the largest for the 60° incidence angle, when calibrated with the reflection characteristics of the aluminium plate.

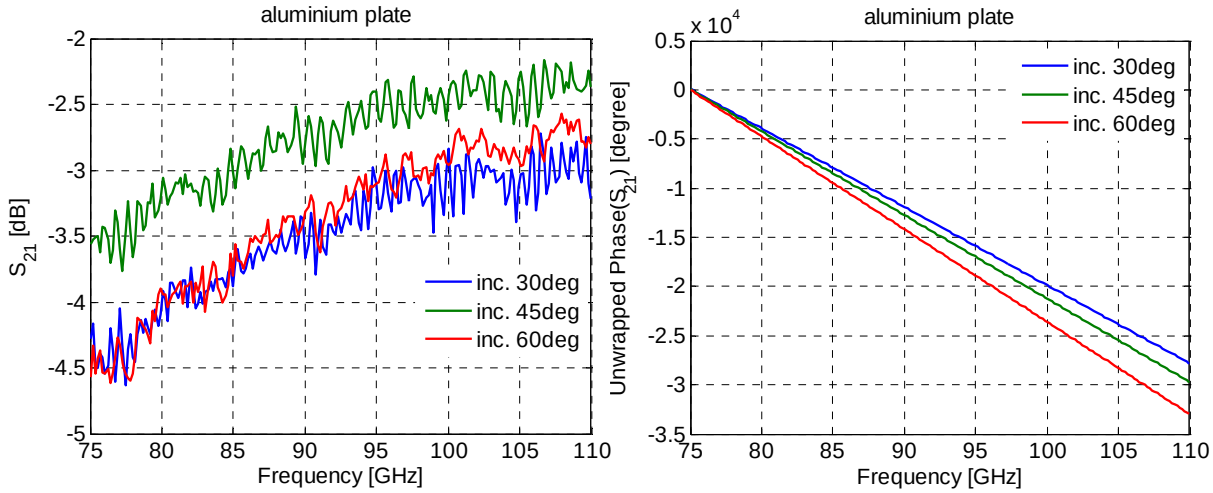

Fig. 12 Comparison of the measured transmission coefficient with different incident angles, aluminum plate as the reflective surface.

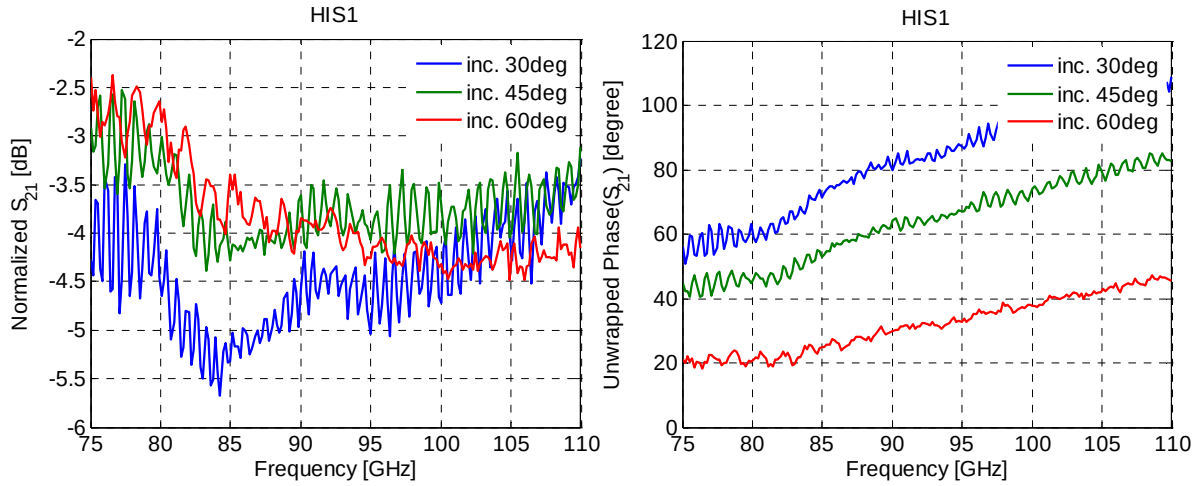

Fig. 13 Comparison of the measured transmission coefficient with different incident angles, HIS1 as the reflective surface (calibration with respect to Al-plate results).

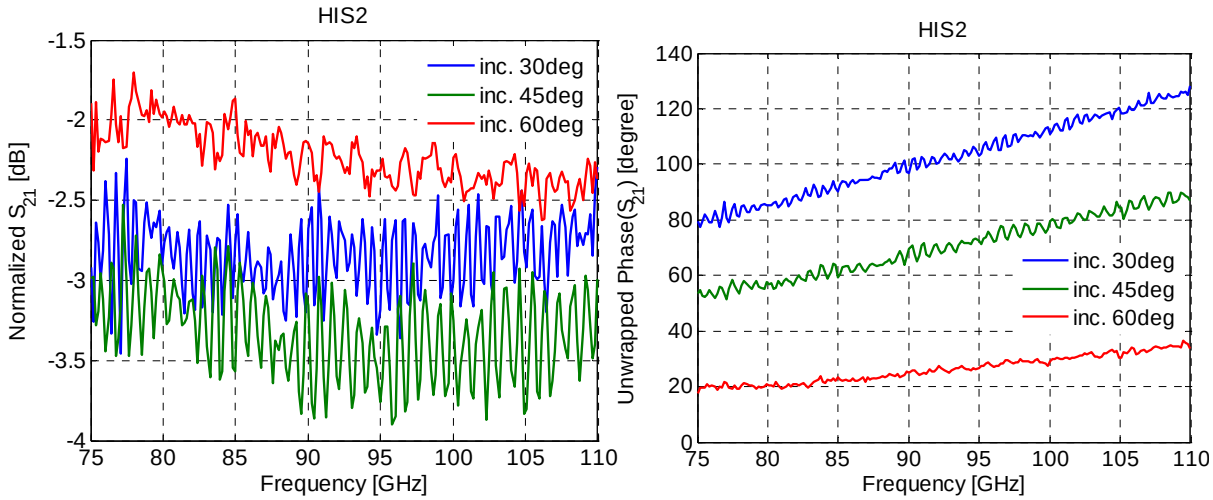

Fig. 14 Comparison of the measured transmission coefficient with different incident angles, HIS2 as the reflective surface (calibration with respect to Al-plate results).

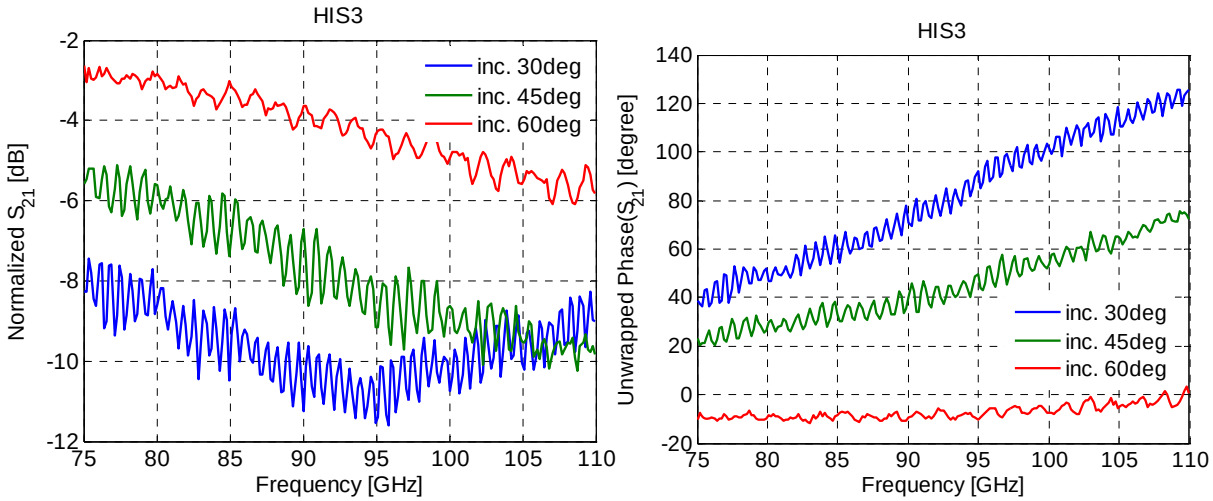

Fig. 15 Comparison of the measured transmission amplitude with different incident angles, HIS3 as the reflective surface (calibration with respect to Al-plate results).

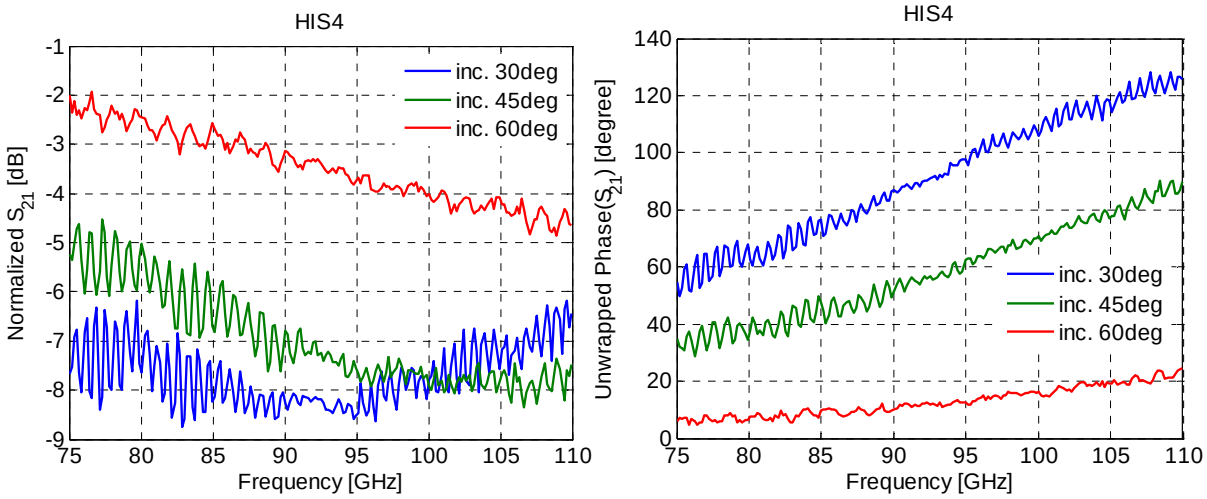

Fig. 16 Comparison of the measured transmission coefficient with different incident angles, HIS4 as the reflective surface (calibration with respect to Al-plate results).

In the measurement results of S21, there are some ripples in the measured amplitude and phase. A Fourier analysis of the measurement results was carried out in order to find out existence of multiple reflections or leakage signals in addition to the desired signal. Fig. 17 shows the results of the inverse Fourier transformed signals in the spatial domain indicating peaks at the path lengths of 0.67 m, 0.71m, and 0.79 m, corresponding to the different measurement geometries for the incidence angles of 30°, 45°, and 60°, respectively. For each case there is an additional signal, which arrives at the receiving horn before the desired signal. These are most probably caused by diffractions from the edges of the parabolic mirrors, holder, or the flat mirror. The levels of these diffraction signals are less than -25 dB compared to the desired signal.

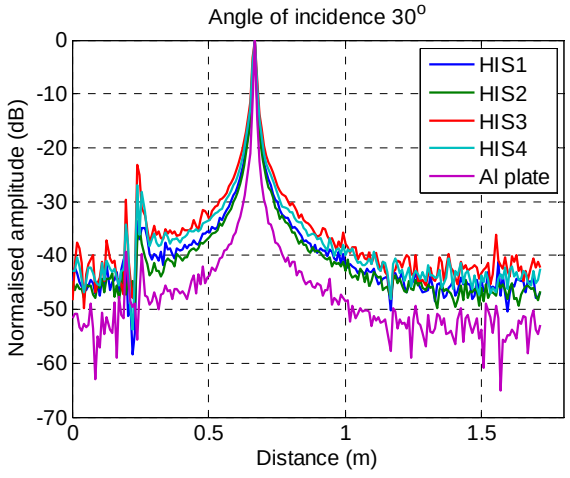

(a)

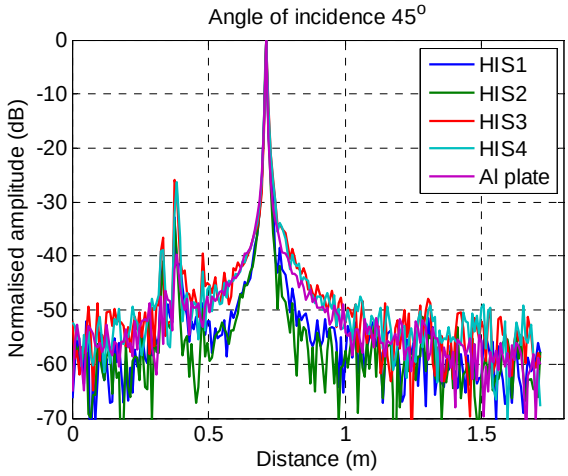

(b)

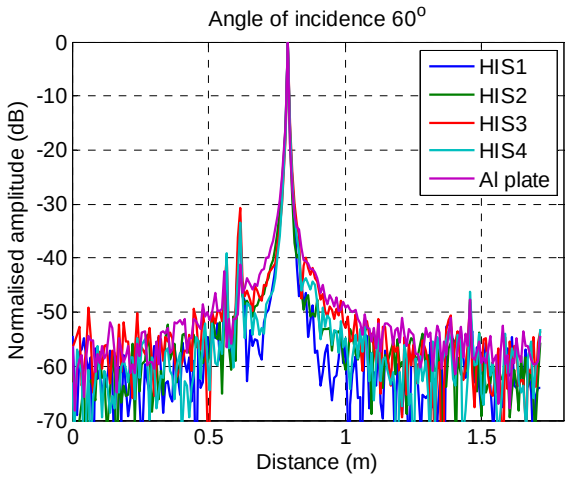

(c)

Fig 17 Inverse Fourier transform of the measured S21 for different incidence angles (a) 30°, (b) 45°, and (c) 60°. Time is multiplied by speed of light in order to present the path length in the *x*-axis.

3.2 Reflection coefficient measurement of the MEMS-based HIS

In addition to the large scale quasi-optical measurements, the reflection coefficients of the HIS samples and aluminum plate are also measured as a backshort of a WR10 waveguide (size of the cross section is 2.54x1.27mm^2), five different positions of the object under test are measured in order to check the repeatablity. Fig. 18 shows the setup of the corresponding measurement.

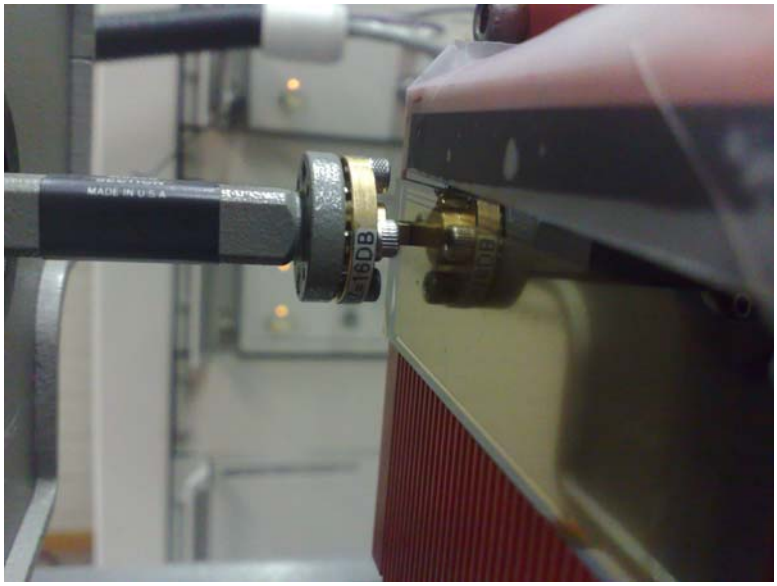

Fig. 18 Photograph of the setup of the S_{11} measurement.

The back-short measurement results are shown in Figs. 19-23. The phase responses are normalized with the calculated phase response of the 10 mm straight WR-10 waveguide section used as the probe. Both the amplitude and phase responses are reasonably flat, thus, these results do not indicate any resonances at the frequency range of the measurements.

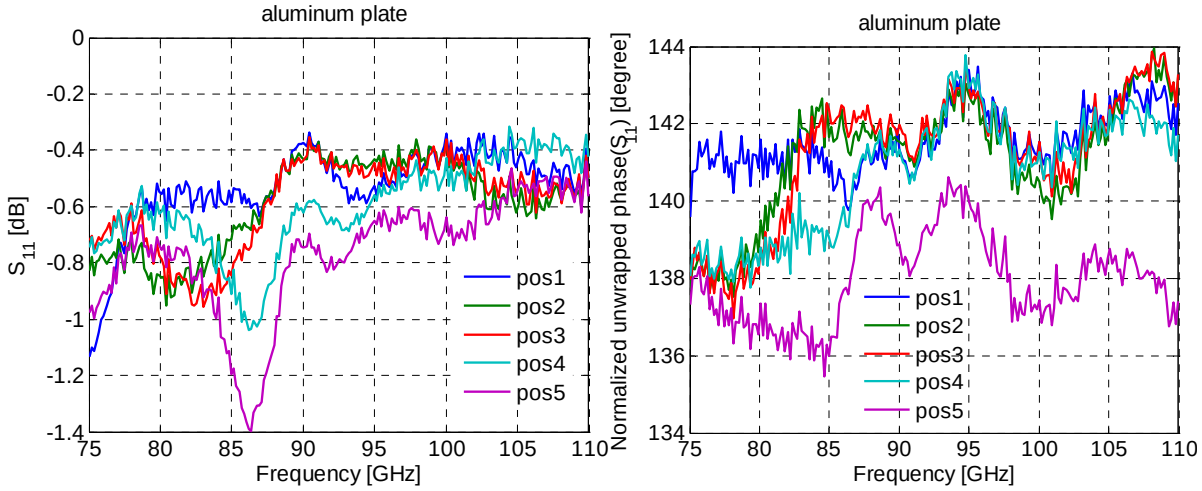

Fig. 19 Measured reflection coefficient of the aluminum plate as a backshort of a WR10 waveguide.

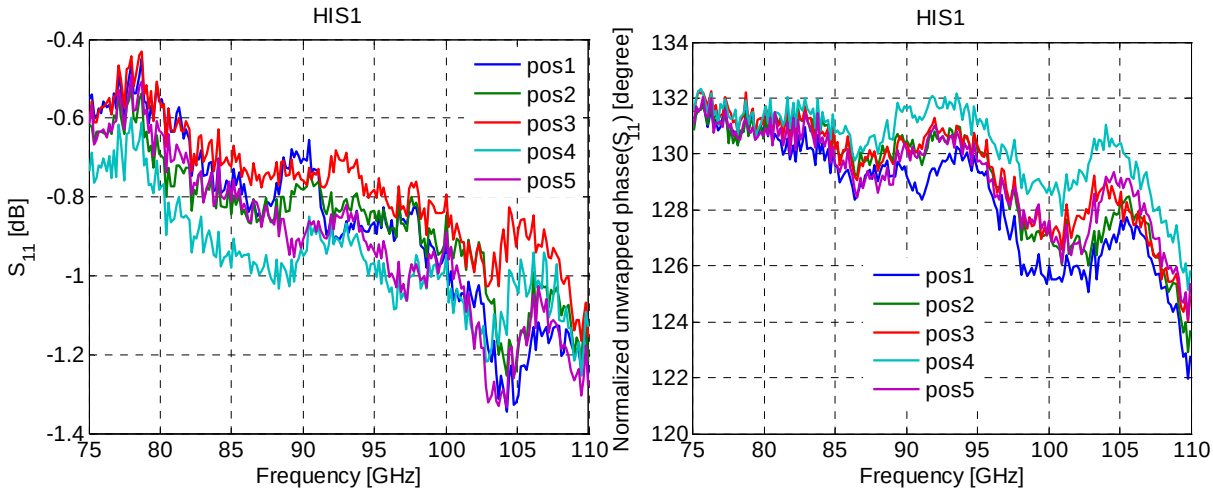

Fig. 20 Measured reflection coefficient of the HIS1 as a backshort of a WR10 waveguide.

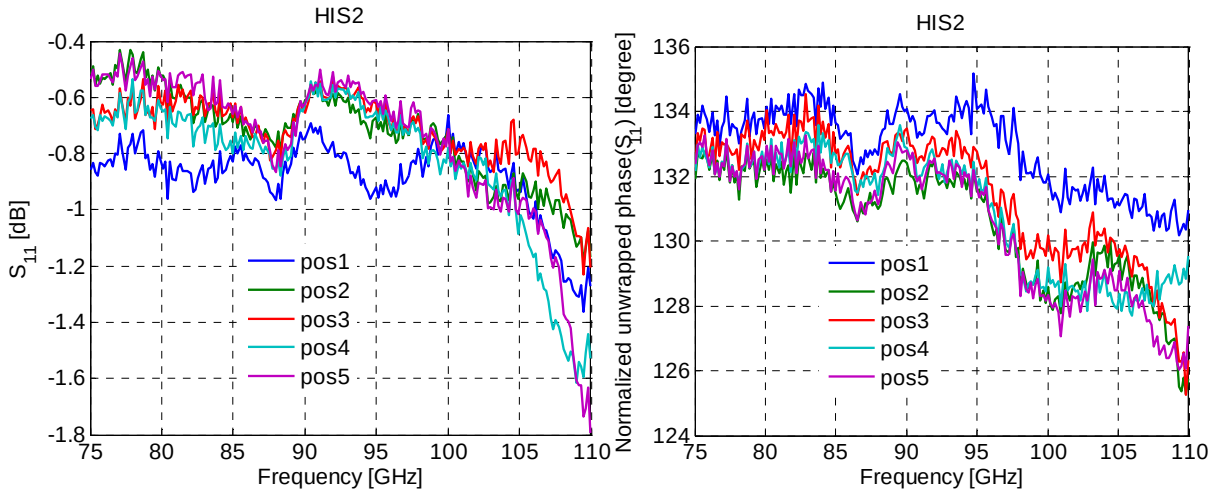

Fig. 21 Measured reflection coefficient of the HIS2 as a backshort of a WR10 waveguide.

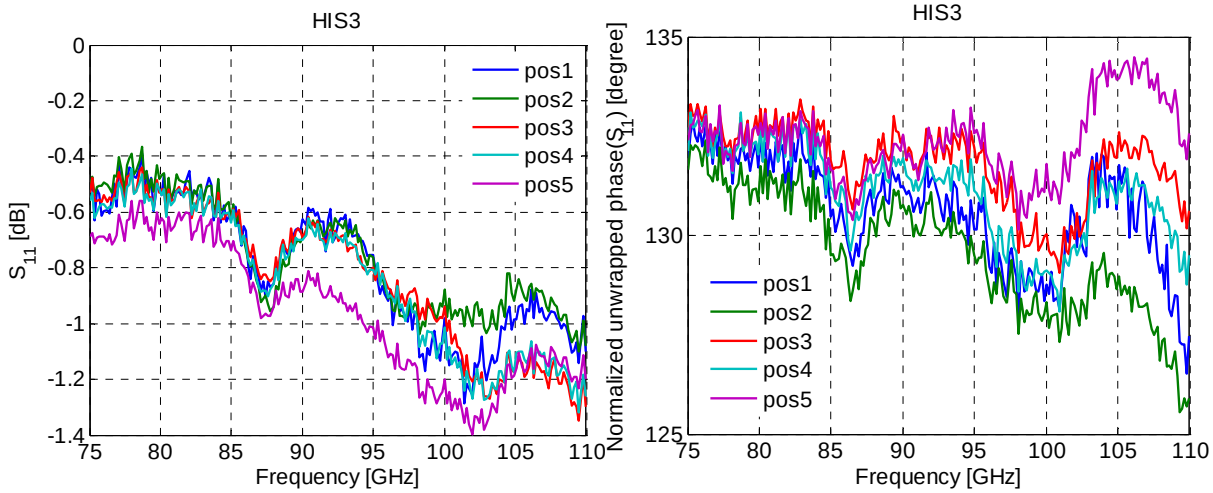

Fig. 22 Measured reflection coefficient of the HIS3 as a backshort of a WR10 waveguide.

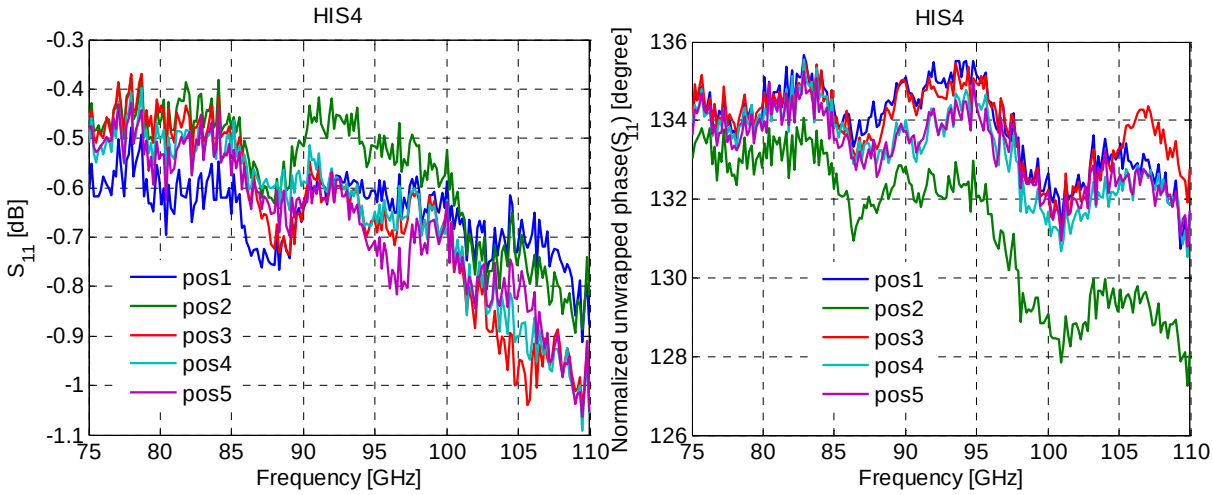

Fig. 23 Measured reflection amplitude of the HIS4 as a backshort of a WR10 waveguide.

4. Measurement of the reflective phase shifter

In addition to the large scale beam steering surfaces a reflective phase shifter chip was fabricated at KTH. The reflective phase shifter chip consists of 5x10 unit cells, the dimensions of which are described in details in deliverable D1.2. Fig. 24 shows the layout of the phase shifter. Red rectangles in the bottom of the figure show the optimal contact areas for the wires to be used for application of the bias voltage. Fig. 25 shows the specially designed WR-12 waveguide mount for the phase shifter chip, and a chip inserted as the backshort of the waveguide. Two contact pads are connected to the membranes and electrodes of the high impedance surface, respectively. Fig 26 indicates the close-up view of the phase shifter chip with the wires clamped to the contact pads.

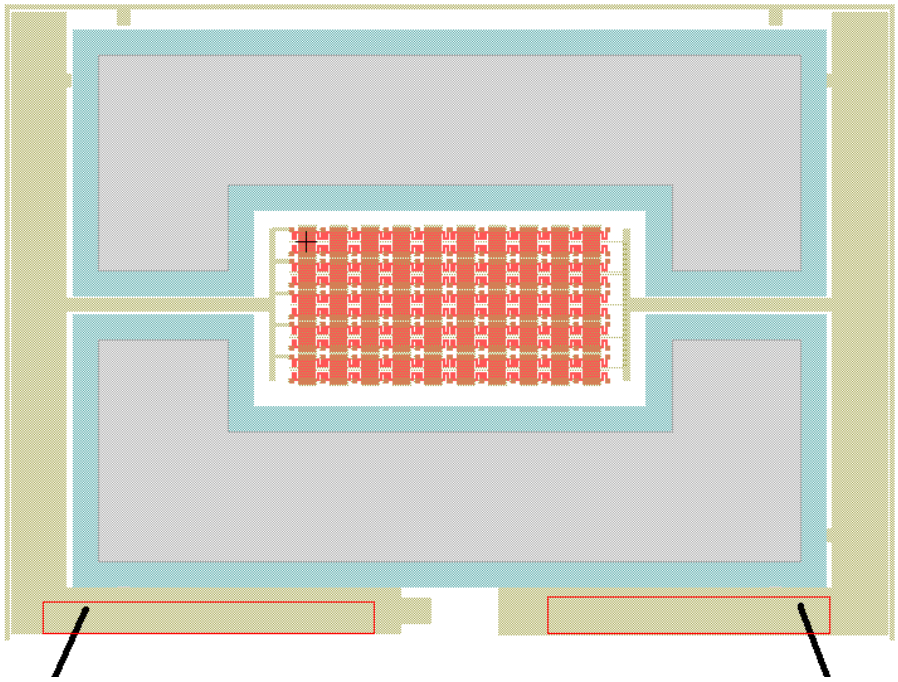

Fig. 24 Layout of the reflective phase shifter.

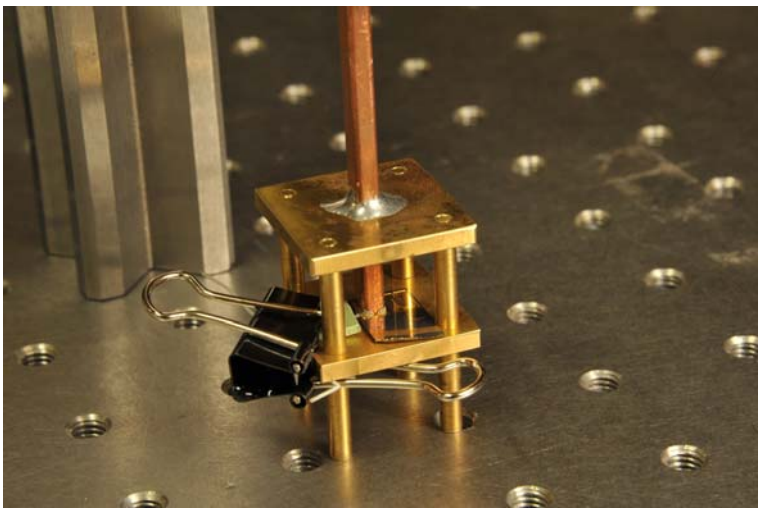

Fig. 25 A reflective phase shifter chip mounted as a backshort of WR-12 waveguide.

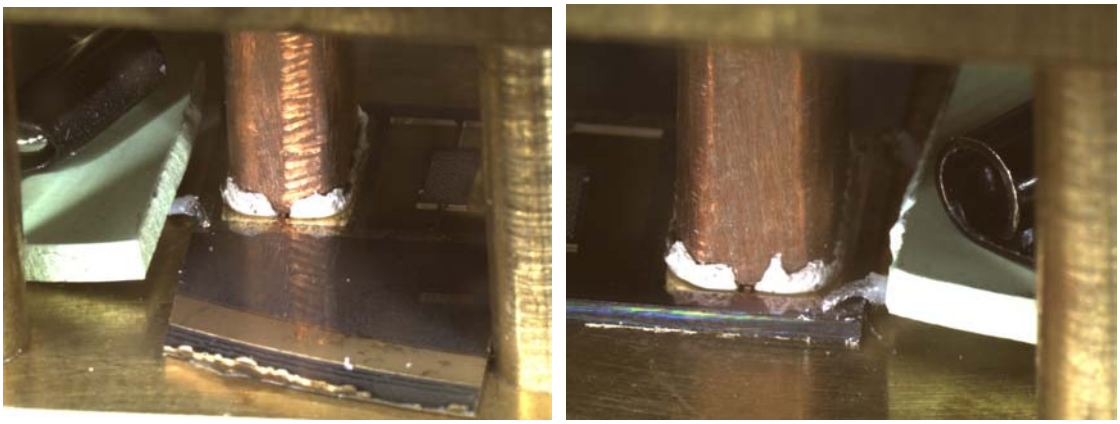

Fig. 26 Close-up view of the wires clamped to the contact pad.

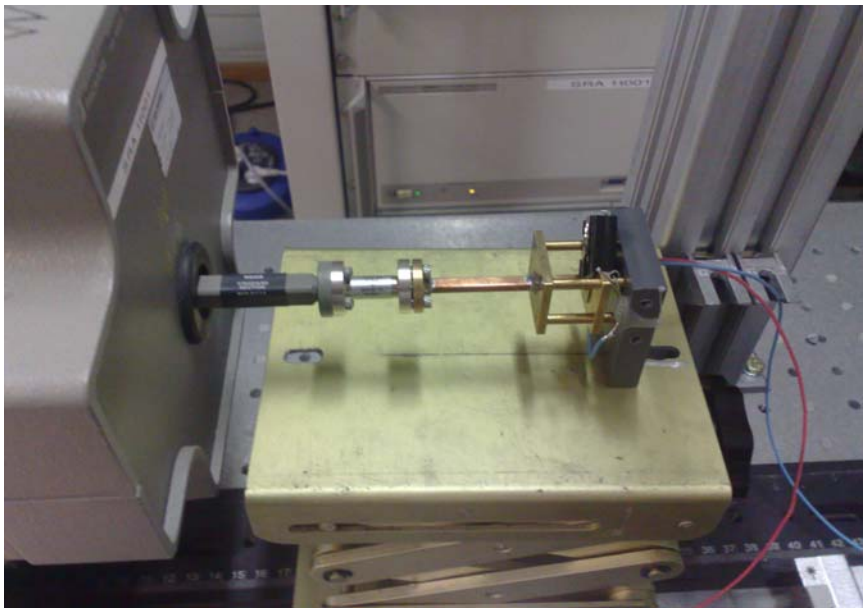

Fig. 27 A WR-10-to-WR-12 transition is connected to the object under test.

A WR10-to-WR12 transition is needed for the phase response measurements with the HP8510 VNA (see Fig 27). Also, the phase shifter chip waveguide mount includes a 57.74 mm-long WR12 waveguide section. Therefore, the phase response of the reflective phase shifter is retrieved from the measured results by subtracting the phase response of the measured WR10-12 waveguide transition and calculated phase response of the 57.74 mm long hollow WR12 waveguide. First the measurement was carried out without applying any biasing voltage. The results are shown in Fig. 28. The measurement results show a resonance frequency of about 91 GHz. The losses at the resonance frequency are about 3 dB when taking into account the WR10-12 transition and the WR-12 waveguide section of the phase shifter mount, Fig. 29 shows the corresponding losses of the WR10-12 transition and 57.74 mm long WR12 waveguide. Outside the resonance frequency the losses are about 0.5-1 dB.

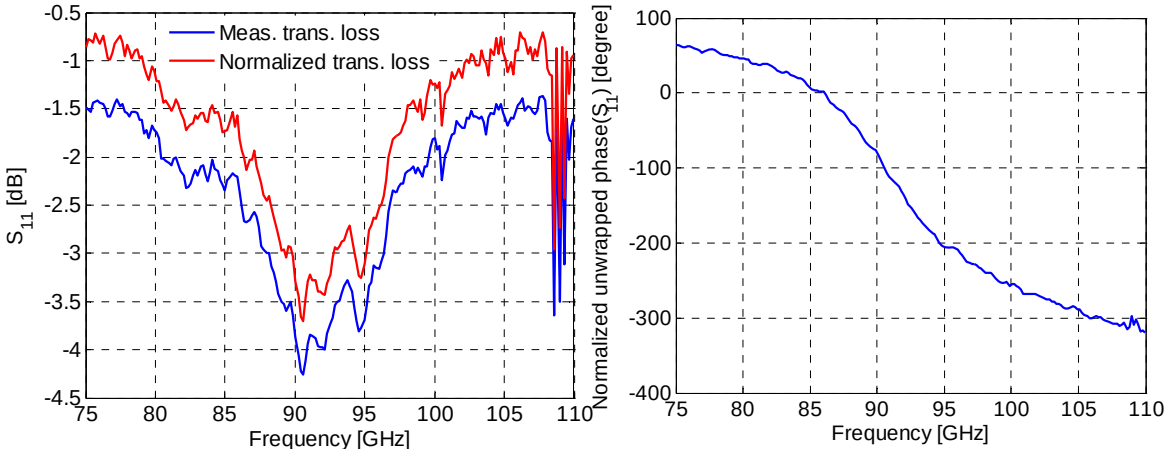

Fig. 28 The comparison of reflection coefficient of the phase shifter as a function of frequency.

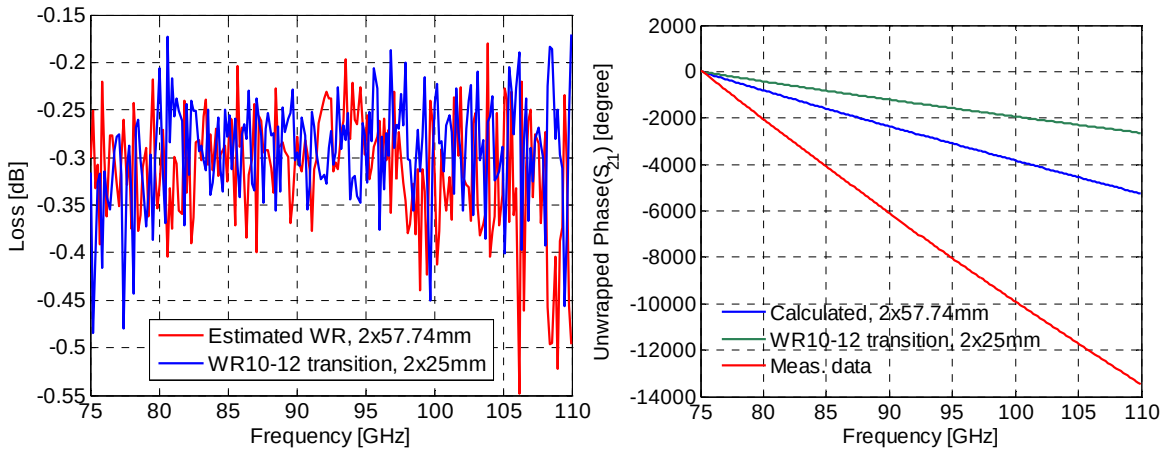

Fig. 29 The comparison of the loss and phase response of the transition and waveguide.

The bias voltage was applied first through wires clamped to the phase shifter contact pads. The measured resistance between the contact pads was about 110 kΩ, which was estimated to be reasonable for the case. A 10 kΩ resistor was assembled in series in order to limit the current in the case of short-circuit. Bias voltages were applied up to about 40 V. However, any change in the reflection coefficient of the phase shifter was noticed. The measured resistance between the waveguide and the voltage contacts were about 10 kΩ and 100 kΩ, respectively, thus possibly implying that the main path for the current is through the waveguide.

In order to improve the contacts, the clamped wires were taken away and two probes mounted on the three-stage micro-manipulators were attached to the contacting pads. Measurement setup with the probes is shown in Figs. 30 and 31. An additional H-plane bend was attached in order to facilitate the probe adjustments. Current meter was also used during the measurement in order to verify the connection resistance while increasing the bias voltage. Table I shows the current variation with the increasing of the bias voltage during the first measurements with the probes. No changes in the response of the phase shifter were observed, when bias voltage was applied.

After re-adjustments of the probes, the measured resistance from probe to probe was about 145 kΩ before actuation. The resistances between the probes and waveguide were 162 kΩ and 96 kΩ (including the additional 10 kΩ resistor). Thus it was expected reasonable contact for the actuation. A bias voltage up to 60 V was applied between the probes, but no changes were observed in the reflection coefficient compared to the case without the bias voltage. After the biasing, the measured resistances were the same as before the measurements. Fig. 32 shows phase response with actuation voltages from 0 to 60 V.

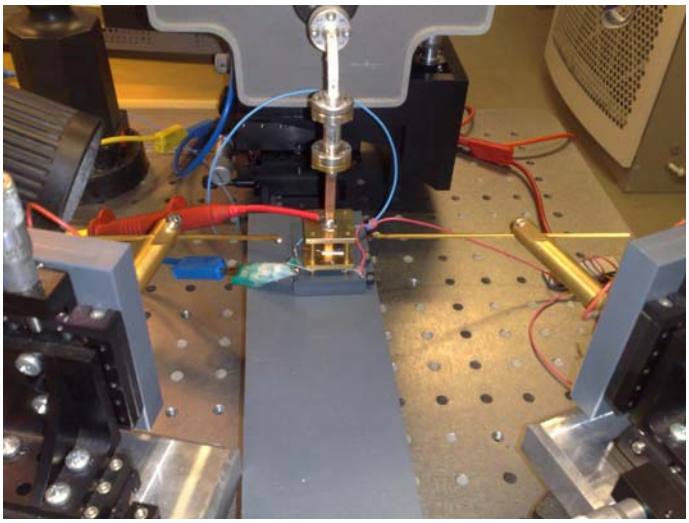

Fig. 30 Setup for the measurement of the tunable phase shifter.

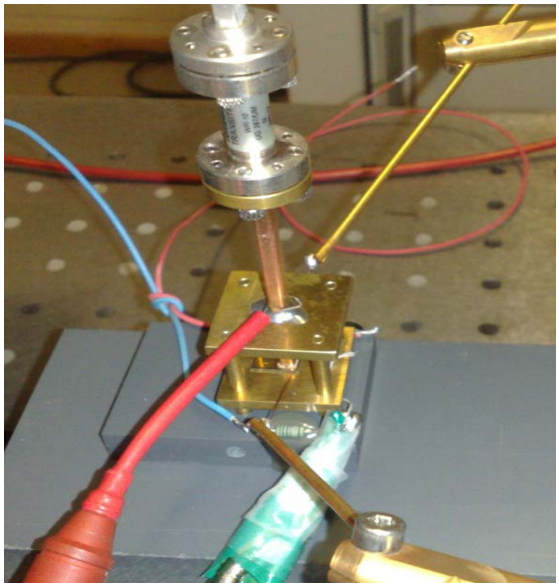

Fig. 31 Close-up view of the probe.

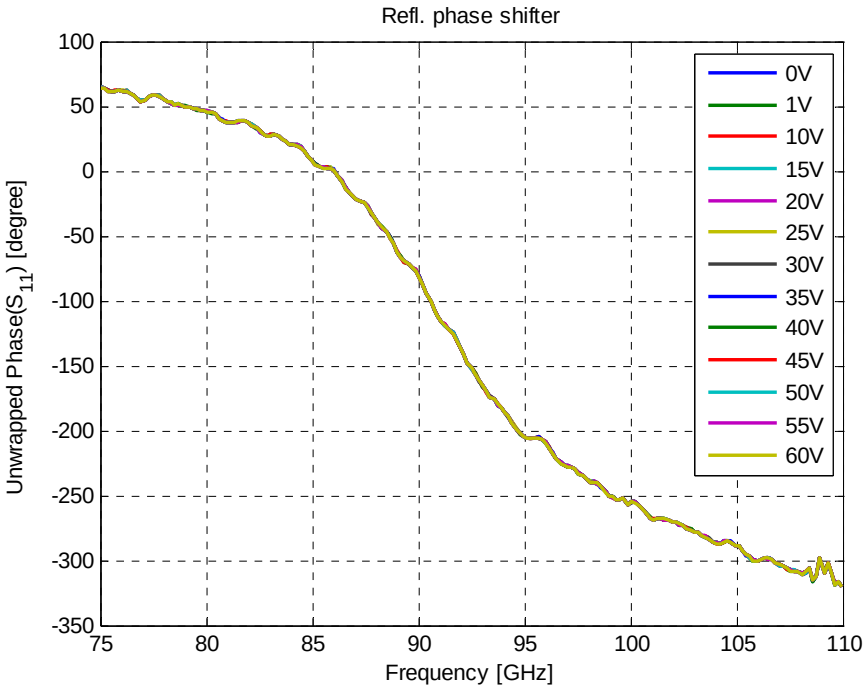

Fig. 32 The phase response of the reflective phase shifter with different biasing voltage.

Table I. Measured voltage and current.

Bias Voltage (V)	Current (mA)	Resistance (kΩ)
1	0.007	143
2	0.014 ~ 0.018	143
5	0.035	143
10	0.062	161
20	0.118	169
30	0.224	134
40	0.400	100

5. Conclusion

The fabrication of the tuneable high-impedance surfaces was not successful during the project because of the limitations in the availability of the optimised processes within the tight time frame at the end of the project. However, four samples were measured in order to find out differences with respect to the incidence angle. The largest specular reflection was observed with the largest angle of incidence (60°).

A reflection type phase shifter based on a MEMS-based high-impedance surface was also characterised. The chip has a resonance frequency at about 91 GHz. The losses at the resonance frequency are about 3 dB, while outside the resonance the losses are about 0.5-1 dB. No changes were observed in the reflection coefficient when applying different bias voltages.